Applied Surface Science 487 (2019) 335–342

Contents lists available at ScienceDirect

Applied Surface Science

journal homepage: www.elsevier.com/locate/apsusc

Full length article

Localized π-conjugated structure and EPR investigation of g-C_3N_4 photocatalyst

Pengfei Xia[a], Bei Cheng[a,*], Jizhou Jiang[b,c,*], Hua Tang[d]

[a] State Key Laboratory of Advanced Technology for Materials Synthesis and Processing, Wuhan University of Technology, 122 Luoshi Road, Wuhan 430070, P.R. China
[b] School of Environmental Ecology and Biological Engineering, Wuhan Institute of Technology, Wuhan 430205, P.R. China
[c] School of Materials Science and Energy Engineering, Foshan University, Foshan 528000, P.R. China
[d] School of Materials Science and Engineering, Jiangsu University, Zhenjiang 212013, P.R. China

ARTICLE INFO

Keywords:
Graphitic carbon nitride
Graphene
Localized π-conjugated structure
Electron paramagnetic resonance (EPR)
Electron spin resonance (ESR)
Hydrogen production

ABSTRACT

The π-conjugated structure of graphitic carbon nitride (g-C_3N_4) is particularly vital to many photocatalytic reactions. Herein, the hybrid structure of tri-s-triazine unit in g-C_3N_4 framework is chemically analyzed and expounded according to the hybrid orbital theory. The localized π-conjugated structure of g-C_3N_4 is also monitored by the electron paramagnetic resonance (EPR) or electron spin resonance (ESR) technique. The experimental results indicate that this π-conjugated structure is attributed to the orbital overlapping of the hybrid carbon and nitride atoms in their $2p_z$ orbits. Unlike graphene with the nonlocalized π-conjugated structure, this orbital overlapping in the whole two-dimensional plane of g-C_3N_4 is separated by the electrons pairs in $2p_z$ orbits of the bridging nitride atoms, leading to the localized π-conjugated structure. Therefore, the g-C_3N_4 exhibits the typical features of a semiconductor with band gap and visible-light response. Meanwhile, the EPR or ESR technique can be acted as the ideal tool to indirectly evaluate the yield of photoelectrons by detecting the superoxide radicals ($\cdot O_2^-$) in g-C_3N_4-based photocatalytic reactions.

1. Introduction

Graphitic carbon nitride (g-C_3N_4) is the promising candidate for metal-free photocatalysts due to its unique electronic structure, visible-light response, environmental benignity, low cost and good chemical stability [1–5]. In this case, it is widely applied in the photocatalytic water splitting, CO_2 reduction, NO_x removal and dye degradation [6–10]. Unlike layered graphene with the nonlocalized π-conjugated structure, the g-C_3N_4 has a localized π-conjugated structure involving the orbital overlap of the hybrid carbon and nitride atoms, which results in the obvious difference with the graphene in the optical properties, electrical and thermal conductivity. In the past several years, many efforts over g-C_3N_4 such as elemental doping, surface modification and heterojunction have been focused on the improvement of dynamic performance of the photogenerated charge carriers such as separation and migration efficiency [11–18]. Nevertheless, few research works investigate the formation mechanism of π-conjugated structure on the intrinsic g-C_3N_4 and the relationship between the photocatalytic performance and the π-conjugated structure still needed to be expounded.

The EPR technique provides a promising non-invasive and non-destructive analytical strategy to detect the paramagnetic species such as the free radicals, transition metal ions, defects, photoelectrons and conjugated structure [19]. Just like the quantized optical absorption of a semiconductor, the unpaired electrons could show the quantized magnetic or microwave absorption. Briefly, the principal energy level of unpaired electron can be split into two separate energy levels with opposite spin orbital momentum under the external magnetic field [20]. This is referred to as the Zeeman interaction between the unpaired electrons and external magnetic field. When it is then exposed to the appropriate microwave radiation or magnetic field, the magnetic dipole transitions could occur and produce paramagnetic resonance absorption [19,20]. The diagram of the paramagnetic resonance absorption of the unpaired electron is described in Fig. 1. The important parameter of the *g* value is the g-factor or Landé-factor, which originates from the spin-orbit coupling interaction and reflects the intrinsic property of each paramagnetic center [19]. In this regard, the *g*-value can be used to identify the specific paramagnetic species.

In this work, the hybrid structure of tri-s-triazine unit in g-C_3N_4 framework is chemically analyzed and explained. The π-conjugated structure is effectively examined by the EPR technique under dark and light conditions. Meanwhile, the superoxide ($\cdot O_2^-$) and hydroxyl

* Corresponding authors.
E-mail addresses: chengbei2013@whut.edu.cn (B. Cheng), 027wit@163.com (J. Jiang).

https://doi.org/10.1016/j.apsusc.2019.05.064
Received 18 January 2019; Received in revised form 11 April 2019; Accepted 7 May 2019
Available online 08 May 2019
0169-4332/

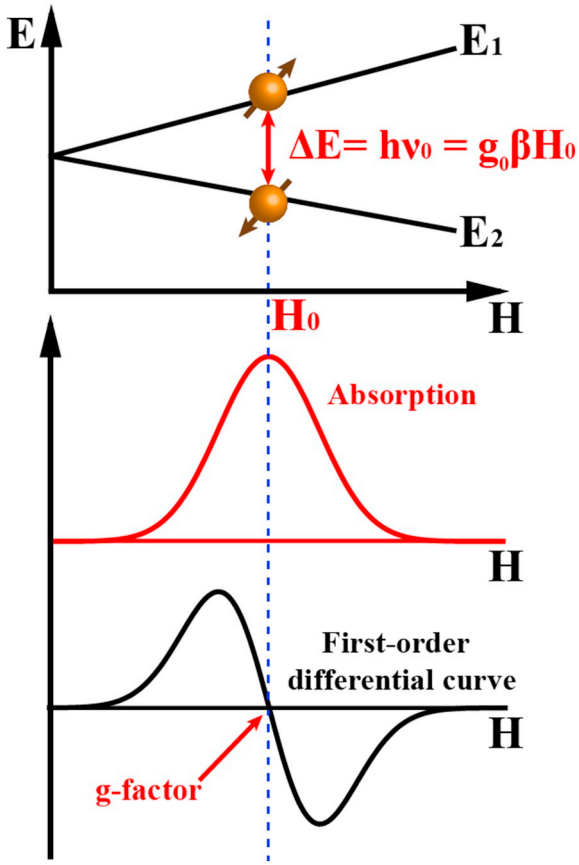

Fig. 1. The schematic diagram of the paramagnetic resonance absorption.

radicals (·OH) are also detected in the photocatalytic reactions of g-C_3N_4.

2. Material and methods

2.1. Synthesis of g-C_3N_4 samples

Typically, 10 g urea was put into a crucible with a cover, which was then placed into a muffle furnace. After that, the urea precursor was heated to 550 °C with the heating rate of 5 °C/min, and keeping this temperature for another 2 h. When the temperature was cooled down to the room temperature, the pale yellow powder was collected and labeled as UCN. Meanwhile, the MCN sample was prepared as above-mentioned processes but the urea precursor was replaced with the melamine. Their preparation processes are described in Fig. 2.

2.2. Characterization of UCN and MCN

Transmission electron microscope (JEM-2100F, JEOL, Japan) was used to obtain TEM images at an accelerating voltage of 200 kV. Nuclear magnetic resonance (NMR) experiments were carried out at 11.7 T on a spectrometer (Bruker-500, Bruker, Germany) using the $^1H \rightarrow {}^{13}C$ CP/MAS NMR technique with the MAS spinning speed of 10 kHz, equipped with a double-resonance 4 mm probe. The $\pi/2$ pulse length for 1H was 4.1 μs, the contact time was 5.5 ms, and the repetition time is 7.0 s. The chemical shifts were referenced to HMB for ^{13}C. X-ray photoelectron spectroscopy (XPS) measurement was carried out in an ultrahigh vacuum VGESCALAB 210 electron spectrometer equipped with a multi-channel detector. The samples were excited by Al Kα (1486.6 eV) radiation (operated at 200 W) of a twin anode in the constant analyzer energy mode with a pass energy of 30 eV. X-ray diffraction (XRD) patterns of the as-prepared samples were obtained on a D/Max-RB X-ray diffractometer (Rigaku, Japan). An IR Affinity-1 FTIR spectrometer (Nicolet iS50, TMO, US) was used to measure the Fourier transform infrared spectra (FTIR). UV–visible diffuse reflectance spectra were recorded on a UV–visible spectrophotometer (UV-2600, Shimadzu, Japan), using $BaSO_4$ as the reference standard. Electron paramagnetic resonance (EPR) was performed on ESR spectrometer (MEX-nano, Bruker) with a modulation frequency of 100 kHz and a microwave power of 15 mW.

2.3. Photocatalytic measurement of H_2 and O_2 production

In a typical experiment, 50 mg of as-prepared photocatalysts were dispersed in 80 mL of deionized water with ultrasonic treatment. After full dispersion of the photocatalysts, the mixed solution was first purged with N_2 for 30 min to remove the air and then irradiated by a 300 W Xe lamp. The hydrogen and oxygen yield were finally analyzed using the gas chromatography (SHIMADZU, Japan).

2.4. Electron paramagnetic resonance (EPR) measurement of UCN and MCN

The as-prepared samples (0.5 g) were encapsulated in a quartz tube with the inner diameter of 4 mm. Next, this tube was slowly inserted into the sample chamber of the EPR spectrometer. The Center Field was set as the 3427 G with the Sweep Width of 200 G. The Receiver Gain, Modulation Amplitude and Attenuation were set as 40 dB, 5G and 35 dB, respectively. The Scan Number and Modulation Frequency were set as the 10 times and 100 kHz, respectively. A LED lamp (λ = 365 nm) was used as the light source to obtain the EPR spectra under light.

2.5. Detection of radicals in the photocatalytic reactions of UCN and MCN

EPR technique was used to detect the free radical species such as hydroxyl radical (·OH) and superoxide radical ($\cdot O_2^-$) with the

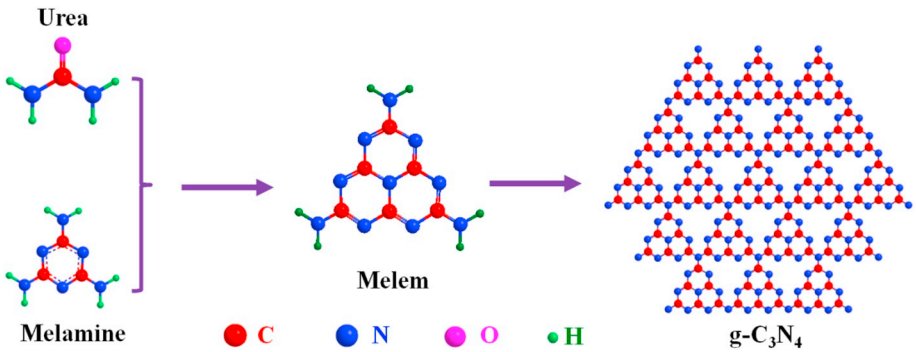

Fig. 2. The formation process of g-C_3N_4 from the thermal condensation of urea and melamine precursors.

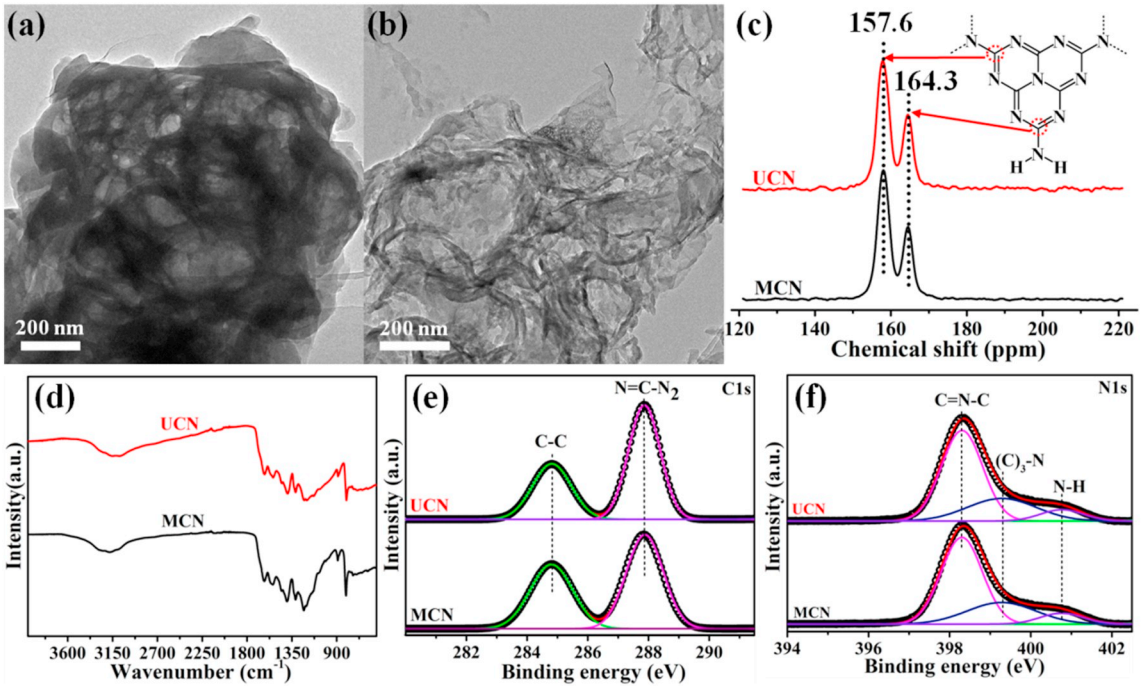

Fig. 3. TEM images of (a) MCN and (b) UCN. (c) NMR, (d) FTIR, (e) C1s high-resolution and (f) N1s high-resolution spectra of UCN and MCN.

assistance of 5,5-Dimethyl-l-pyrroline N-oxide (DMPO). Specifically, for the detection of hydroxyl radical (·OH), the as-prepared sample was dispersed into deionized water to form the 2.5 mg/mL suspension under the ultrasonic conditions. Subsequently, 50 μL DMPO was added into above suspension under the rapidly stirring. Then, this mixture was irradiated for 120 s using a 300 W Xe lamp under the rapid agitation. After that, the supernatant of above mixture was quickly sampled and tested in the EPR equipment. Additionally, the detection procedure of superoxide radical ($\cdot O_2^-$) was same with that of hydroxyl radical (·OH), except that the deionized water was replaced as the methanol.

2.6. Calculation of density of states (DOS)

Density functional theory (DFT) calculations were carried out using the exchange–correlation function and CASTEP module. The HSE06 hybrid functional was used to obtain the band structure. An energy cutoff of 450 eV was used to perform geometry optimization and electronic property calculations. The energy and force convergence criteria were set as 1.0×10^{-5} eV per atom and 0.03 eV $Å^{-1}$, respectively.

3. Results and discussion

The morphologies of the MCN and UCN are examined by the TEM, as shown in Fig. 3a and b, respectively. The TEM image of MCN in Fig. 3a shows the bulk structure with pore, whereas the UCN in Fig. 3b exhibits the nanosheet-like structure. Although their morphologies is obviously different, the NMR of ^{13}C, FTIR and XPS spectra of UCN sample are the same as those of MCN as presented in Fig. 3(c–f), respectively. More specifically, for their NMR spectra, the chemical shifts at 157.6 and 164.3 ppm are attributed to the sp^2 hybrid carbon (N = C-N_2) and terminal carbon (C-NH_2) atoms of the tri-s-triazine ring, respectively [21]. Meanwhile, for their FTIR spectra in Fig. 3d, the peak at 810 and 1200–1600 cm^{-1} can be assigned to the breathing vibration of the tri-s-triazine ring and various vibrations of C—N bonds, respectively [2,22–25]. For their XPS spectra in Fig. 3e and f, their high-resolution C1s XPS spectra are fitted into two peaks at 284.6 and 287.8 eV, which can be attributed to the externally adsorbed carbon species and the sp^2 hybrid carbon atoms (N = C-N_2) in the tri-s-triazine ring, respectively [26–28]. Correspondingly, their high-resolution N1s XPS spectra can be fitted into three peaks at 398.3, 399.5 and 400.8 eV, which can be indexed as the inner nitride atoms (C = N-C), bridging nitride atoms (N-$(C)_3$) and nitride atoms of the terminal amino group (-NH or -NH_2), respectively [29–31]. No difference in their NMR, FTIR and XPS spectra can be found, suggesting that both UCN and MCN have the identical chemical composition and basic structural unit of tri-s-triazine rings.

The XRD patterns are measured to probe their crystal structure, as shown in Fig. 4a. The peak at 13.1°, corresponding to (100) plane, originates from the periodic stacking of tri-s-triazine rings. Another peak can be assigned to the (002) plane, which is ascribed to the periodic stacking of the interlaminations [32–35]. Noted that the (002) peak of UCN slightly shifts lower diffraction angle than that of MCN, suggesting that the nanostructured UCN could weaken Vander Waals' interaction existing in the interlaminations of g-C_3N_4. The optical properties of UCN and MCN are investigated by the UV–visible DRS, as shown in Fig. 4b. The absorption band edges of UCN and MCN are 443 and 454 nm, corresponding to the band gap of 2.82 and 2.73 eV, respectively. It is noted that the absorption band edge of UCN exhibits a small blue shift in comparison with that of MCN, which is attributed to the quantum size effect of nanostructured UCN [6,36–39]. Additionally, their valence band (VB) positions can be obtained from the XPS valence spectra, as presented in Fig. 4c [2,12,40]. The VB positions of UCN and MCN are 1.42 and 1.36 eV, respectively. According to their measured band gaps and VB positions, the conduction band (CB) positions of UCN and MCN can be calculated to be −1.40 and −1.37 eV, respectively. Thus, their band structure can be summarized in Fig. 4d, which indicates that both UCN and MCN could thermodynamically split water to produce hydrogen and oxygen under the light irradiation.

In order to investigate the electronic structure of g-C_3N_4, the hybridization analysis of carbon and nitride atoms in the tri-s-triazine ring of g-C_3N_4 is performed and presented in Figs. 5 and 6. For the carbon atom (N = C-N_2) of the tri-s-triazine ring in the ground state, its 2s orbit is fully filled with two electrons of opposite spin orientation. Meanwhile, its 2p orbit can be split into three sub orbits of $2p_x$, $2p_y$ and $2p_z$, the first two of which are filled with the unpaired electron and the $2p_z$ sub orbit has no filled electron. After excited, the $2p_x$, $2p_y$ and $2p_z$ orbits

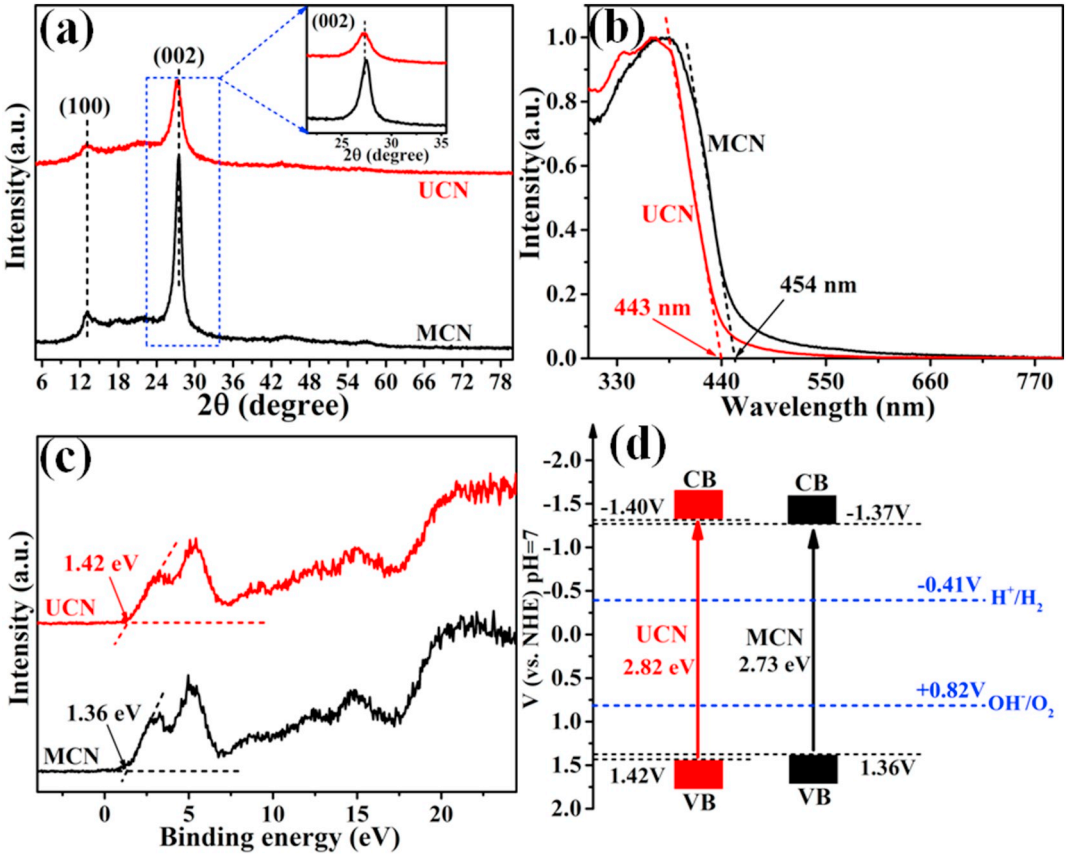

Fig. 4. (a) XRD patterns, (b) UV–vis spectra, (c) XPS valence-band spectra and (d) band structures of UCN and MCN.

are filled with the unpaired electron with the same spin orientation. Then, this 2s orbit could hybridize with the $2p_x$ and $2p_y$ sub orbits to form three sp^2 equivalent hybridization (EH) orbits, leaving the $2p_z$ sub orbit with the unpaired electron. This hybrid process can be described in Fig. 5a. Additionally, for the nitride atom (C-N=C) in the ground state, its 2s orbit is fully filled with two electrons of opposite spin orientation and its 2p orbit can also be split into three sub orbits of $2p_x$, $2p_y$ and $2p_z$. After excited, the $2p_x$ and $2p_y$ sub orbits are filled with the unpaired electron and two electrons of opposite spin orientation, respectively. Then, its 2s orbit could hybridize with the $2p_x$ and $2p_y$ sub orbits to form three sp^2 nonequivalent hybridization (NEH) orbits, leaving the $2p_z$ sub orbit with the unpaired electron, which can be described in Fig. 5b. Moreover, another bridging nitride atom (N-$(C)_3$) is also sp^2 equivalent hybridization (EH) as described in Fig. 5c. Its hybrid process is similar to that of the equivalent hybrid carbon atom (N=C-N_2), but the difference is that its $2p_z$ sub orbit is fully filled with two electrons with opposite spin orientation.

After hybridization of carbon and nitride atoms, their hybrid sp^2 orbits overlap each other to form σ-type bonds, whereas their overlapping $2p_z$ sub orbits form π-type bonds. It is well known that the

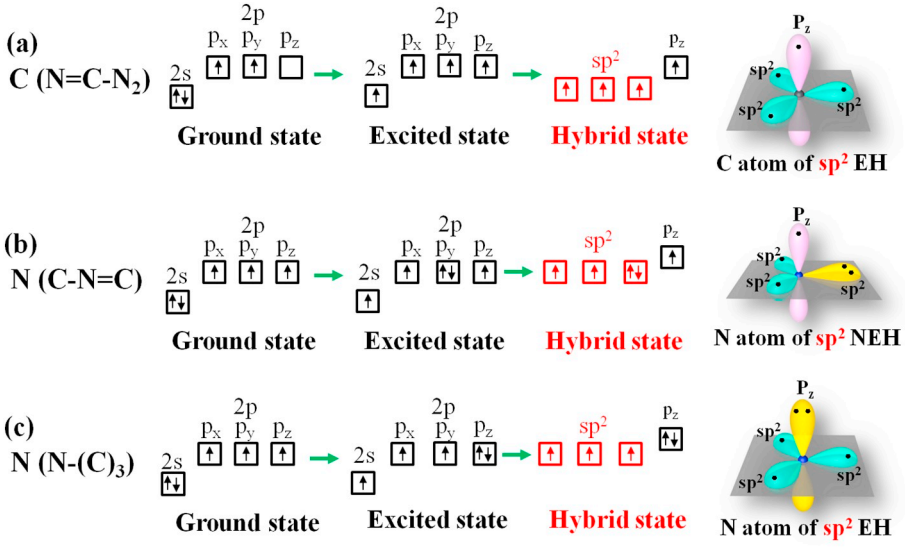

Fig. 5. The hybrid analysis of carbon and nitride atoms in the tri-s-triazine of g-C_3N_4.

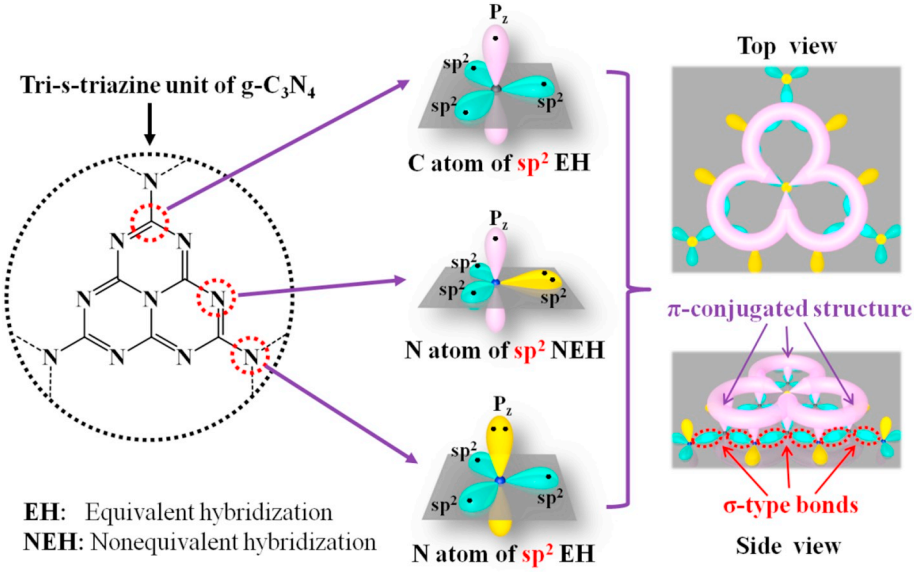

Fig. 6. Hybrid structure and π-conjugated structure of the tri-s-triazine unit of g-C_3N_4.

electrons in the π-type bonds cannot be confined in the specific atoms but move freely in all π-type bonds to form π-conjugated structure. In this π-conjugated structure, half of electrons are from the $2p_z$ sub orbit of carbon atoms and the residual electrons are from the $2p_z$ sub orbit of nitride atoms.

Contrarily, the electron pair with opposite spin orientation in the $2p_z$ sub orbit of the equivalent hybridization nitride atoms (bridging nitride atoms or (N-$(C)_3$)) does not participate in above mentioned π-conjugated structure because of the Coulomb repulsion caused by the electrons with different spin orientations. In this case, the electrons in the π-conjugated structure cannot move through the whole two-dimensional plane of g-C_3N_4 but move freely within the specific tri-s-triazine ring, leading to a localized π-conjugated structure as presented in Fig. 6. This localized π-conjugated structure in the tri-s-triazine ring of g-C_3N_4 can be clearly presented by its spherical aberration-corrected STEM images performed by Yu and coworkers in their previous report [8]. The high-resolution STEM image on the atomic scale shows that the electron concentration is separated by the bridging nitride atoms (N-$(C)_3$) and mainly confined within the tri-s-triazine rings. Just like N-doped graphene, this localized π-conjugated structure endows the g-C_3N_4 materials with poor electrical and thermal conductivity but good semiconductor-related properties such as visible-light response and much negative VB potential [21,41–43].

To further understand the localized π-conjugated structure of g-C_3N_4, the EPR technique is used to detect the paramagnetic species of g-C_3N_4, as shown in Fig. 7a. The EPR spectra measured in darkness over the UCN and MCN samples exhibit the single Lorentzian line with the g-factor of 2.0053, indicating that both UCN and MCN contain only one kind of paramagnetic species. According to the above analysis and discussion, this paramagnetic species of the g-C_3N_4 are only from the unpaired electrons in the localized π-conjugated structure rather than the electron pairs in σ-type bonds and $2p_z$ sub orbit of bridging nitride atoms. This is because these electron pairs have the counteracting spin magnetic moment and cannot produce the paramagnetic resonance absorption [44,45]. It is noted that the intensity of EPR signal over the UCN is higher than that of MCN, which is attributed to more defects in nanostructured UCN than bulk MCN. When the UCN and MCN samples are exposed under illumination, their EPR signals obviously increase but the g-factor remains unchanged in comparison with the results measured in darkness. This result indicates that their localized π-conjugated structures receive certain new paramagnetic species under illumination, which has been confirmed to be the photoelectrons in previous reports [3,46].

The density of state (DOS) is helpful and necessary to understand the electronic properties as shown in Fig. 7b. Although the DOS cannot give the information of 2p sub orbits, it still can be used for the qualitative analysis for the composition of VB and CB [47–50]. After calculation of DOS, it is noted that the VB of UCN and MCN consists of 2s and 2p orbits of carbon and nitride atoms, which is coincident with the ingredients of their sp^2 hybrid orbits. Meanwhile, the CB of UCN and MCN is composed of approximate half 2p orbits of carbon atoms and nitride atoms, which is in good accordance with the ingredients of their localized π-conjugated structures. In this regard, it can reasonably infer that the electrons can transfer to the π-conjugated structure from the σ-type bonds under illumination, as presented in Fig. 7c, corresponding to the fact that the electrons from VB of g-C_3N_4 transfer to the CB to form the photoelectrons under the light irradiation.

The photocatalytic pure water splitting is used to evaluate the photocatalytic activity of UCN and MCN as shown in Fig. 8a. The rates of photocatalytic H_2 production of UCN and MCN are 53 and 21 $\mu mol\, h^{-1}\, g^{-1}$, respectively. The rates of photocatalytic O_2 production of UCN and MCN are 19 and 6 $\mu mol\, h^{-1}\, g^{-1}$, respectively. Both UCN and MCN as the pristine g-C_3N_4 show very poor photocatalytic performance, which is attributed to the high recombination rate of photogenerated charge carriers [51–54]. It is noted that the photocatalytic activity of UCN is higher than that of MCN, this is because the UCN can produce more photoelectrons than that of MCN under illumination, as confirmed by EPR measurement.

Furthermore, the superoxide ($\cdot O_2^-$) and hydroxyl ($\cdot$OH) radicals are monitored by the EPR technique as presented in Fig. 8b and c, respectively. In Fig. 8b, the blank experiments cannot detect the any EPR signal of radicals, suggesting that the 5,5-Dimethyl-l-pyrroline N-oxide (DMPO) has no paramagnetic center and the g-C_3N_4 photocatalyst cannot produce the radicals without illumination. When the photocatalytic systems of UCN and MCN are exposed under illumination, their EPR spectra show the four peaks with approximate intensity, which can be attributed to the typical paramagnetic resonance absorption of DMPO-$\cdot O_2^-$ adducts. This result indicates that both UCN and MCN can thermodynamically produce the superoxide ($\cdot O_2^-$) radicals under illumination because their CB positions are more negative than the potential of $O_2/\cdot O_2^-$ (−0.33 V, NHE) [55–58]. Additionally, it is noted that the EPR signal intensity of UCN is higher than that of MCN, indicating that the photoelectron concentration in the localized π-conjugated structure of UCN is higher than that of MCN under

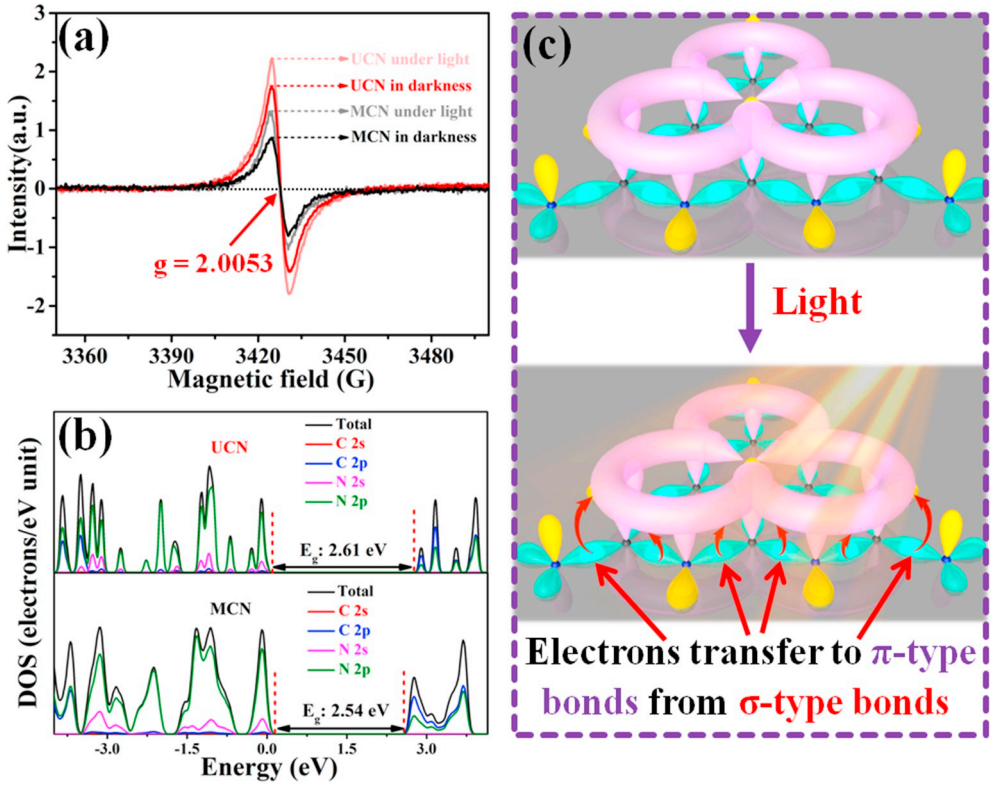

Fig. 7. (a) EPR spectra of UCN and MCN in darkness and under illumination. (b) The diagram of π-conjugated structure and electron transfer process in the tri-s-triazine unit under illumination. (c) The DOS of UCN and MCN.

illumination based on the abovementioned discussion. This result is consistent with that of photocatalytic H_2 production, indicating that the photogenerated electrons in g-C_3N_4 have enough reduction ability. As expected, the hydroxyl (·OH) radicals cannot be detected in both UCN and MCN photocatalytic systems, as presented in Fig. 8c. The above experimental results show that both UCN and MCN can produce the O_2

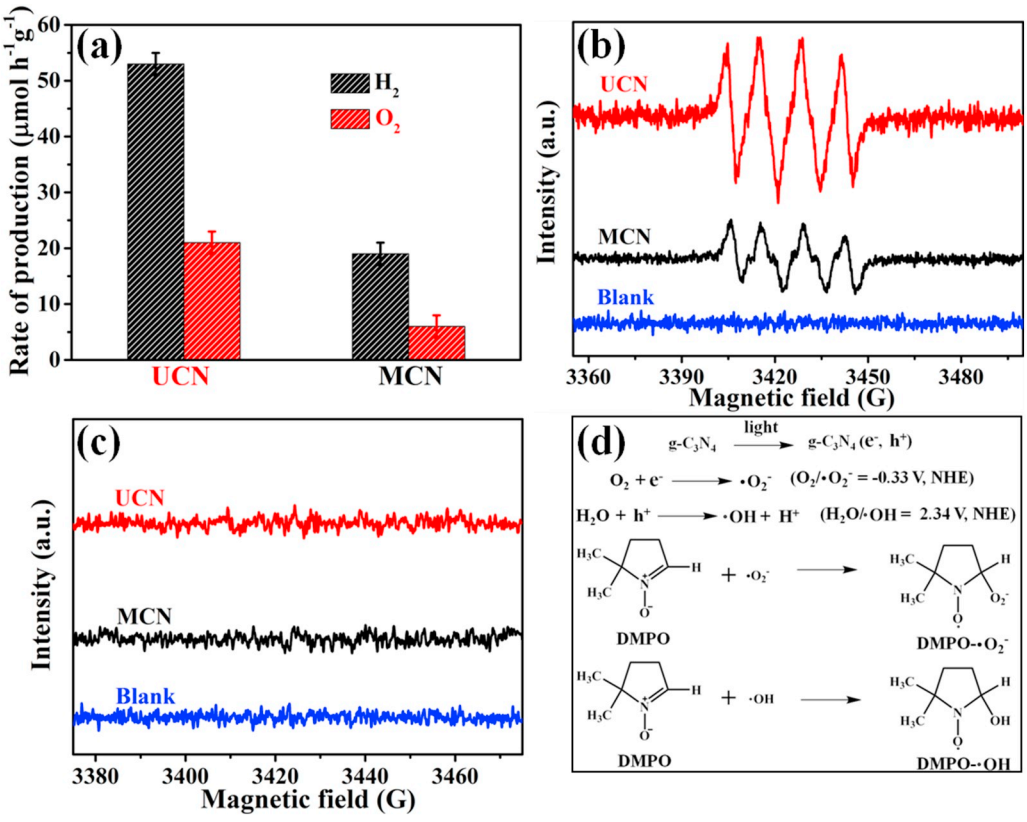

Fig. 8. (a) The production rate of H_2 and O_2 towards the UCN and MCN under illumination. (b) The EPR signals of DMPO-·O_2^- adducts in the photocatalytic system of UCN, MCN and blank experiment after illumination for 120 s. (c) The EPR signals of DMPO-·OH adducts in the photocatalytic system of UCN, MCN and blank experiment after illumination for 120 s. (c) The formation mechanism of the free radicals and corresponding adducts in the EPR trapping experiments.

but cannot produce the hydroxyl (·OH) radicals under illumination. This is because the VB positions of UCN and MCN is more positive than potential of H_2O/O_2 (0.82 V, NHE) but less positive than the potential of $H_2O/·OH$ (2.34 V, NHE), as shown in Fig. 8d [59–62].

4. Conclusions

In summary, two kinds of g-C_3N_4 are prepared by thermal polycondensation of urea and melamine precursors, respectively. The localized π-conjugated structure of g-C_3N_4 is detected and expounded in darkness and under illumination. According to the hybrid analysis of the tri-s-triazine unit in g-C_3N_4 and the EPR examination, the π-conjugated structure of g-C_3N_4 is confirmed to be the localized π-conjugated structure, which leads to the semiconductor properties of band gap and visible-light response. Under illumination, the electrons can migrate to the π-conjugated structure from the σ-type bonds, leading to the production of photoelectrons. Additionally, by detecting the superoxide radicals ($·O_2^-$) in the g-C_3N_4-based photocatalytic reactions and the intrinsic signal intensity of g-C_3N_4 under illumination using the EPR technique, a new approach is developed to examine the photoelectron concentration of g-C_3N_4 under illumination, which can be used to indirectly evaluate the photocatalytic H_2-production activity. This work provides a new insight into π-conjugated structure of g-C_3N_4 and evaluation method of photocatalytic activity.

Acknowledgments

This work was supported by the Natural Science Foundation of China (21433007, 21573170, U1705251 and 21871217), National Postdoctoral Program for Innovative Talents (BX20190309), National Key Research and Development Program of China (2018YFB1502001) and Innovative Research Funds of SKLWUT (2017-ZD-4).

References

[1] W.J. Ong, L.L. Tan, Y.H. Ng, S.T. Yong, S.P. Chai, Graphitic carbon nitride (g-C_3N_4)-based photocatalysts for artificial photosynthesis and environmental remediation: are we a step closer to achieving sustainability? Chem. Rev. 116 (2016) 7159–7329.
[2] J. Fu, Q. Xu, J. Low, C. Jiang, J. Yu, Ultrathin 2D/2D WO_3/g-C_3N_4 step-scheme H_2-production photocatalyst, Appl. Catal. B-Environ. 243 (2019) 556–565.
[3] Y.F. Li, R.X. Jin, Y. Xing, J.Q. Li, S.Y. Song, X.C. Liu, M. Li, R.C. Jin, Macroscopic foam-like holey ultrathin g-C_3N_4 nanosheets for drastic improvement of visible-light photocatalytic activity, Adv. Energy Mater. 6 (2016) 1601273.
[4] A. Nikokavoura, C. Trapalis, Graphene and g-C_3N_4 based photocatalysts for NO_x removal: a review, Appl. Surf. Sci. 430 (2018) 18–52.
[5] E. Liu, J. Chen, Y. Ma, J. Feng, J. Jia, J. Fan, X. Hu, Fabrication of 2D SnS_2/g-C_3N_4 heterojunction with enhanced H_2 evolution during photocatalytic water splitting, J. Colloid Interf. Sci. 524 (2018) 313–324.
[6] P. Xia, B. Zhu, J. Yu, S. Cao, M. Jaroniec, Ultra-thin nanosheet assemblies of graphitic carbon nitride for enhanced photocatalytic CO_2 reduction, J. Mater. Chem. A 5 (2017) 3230–3238.
[7] Z. Liu, G. Wang, H.S. Chen, P. Yang, Amorphous/crystalline g-C_3N_4 homojunction for visible light photocatalysis reaction with superior activity, Chem. Commun. 54 (2018) 4720–4723.
[8] W. Yu, J. Chen, T. Shang, L. Chen, L. Gu, T. Peng, Direct Z-scheme g-C_3N_4/WO_3 photocatalyst with atomically defined junction for H_2 production, Appl. Catal. B-Environ. 219 (2017) 693–704.
[9] L. Ni, Z. Jing, Z. Sheng, X. Wei, Molten salt-mediated formation of g-C_3N_4-MoS_2 for visible-light-driven photocatalytic hydrogen evolution, Appl. Surf. Sci. 430 (2017) 218–224.
[10] Z.J. Wang, Z.L. Jin, H. Yuan, G.R. Wang, B.Z. Ma, Orderly-designed Ni_2P nanoparticles on g-C_3N_4 and UiO-66 for efficient solar water splitting, J. Colloid Interf. Sci. 532 (2018) 287–299.
[11] H. Zhang, F. Liu, Z. Mou, X. Liu, J. Sun, W. Lei, A facile one-step synthesis of ZnO quantum dots modified poly(triazine imide) nanosheets for enhanced hydrogen evolution under visible light, Chem. Commun. 52 (2016) 13020–13023.
[12] P. Xia, B. Zhu, B. Cheng, J. Yu, J. Xu, 2D/2D g-C_3N_4/MnO_2 nanocomposite as a direct Z-scheme photocatalyst for enhanced photocatalytic activity, ACS Sustain. Chem. Eng. 6 (2017) 956–973.
[13] H. Jung, T. Pham, E. Shin, Interactions between ZnO nanoparticles and amorphous g-C_3N_4 nanosheets in thermal formation of g-C_3N_4/ZnO composite materials: the annealing temperature effect, Appl. Surf. Sci. 458 (2018) 369–381.
[14] Q. Xu, L. Zhang, J. Yu, S. Wageh, A. Al-Ghamdi, M. Jaroniec, Direct Z-scheme photocatalysts: principles, synthesis, and applications, Mater. Today 21 (2018) 1042–1063.
[15] K. He, J. Xie, M. Li, L. Xin, In situ one-pot fabrication of g-C_3N_4 nanosheets/NiS cocatalyst heterojunction with intimate interfaces for efficient visible light photocatalytic H_2 generation, Appl. Surf. Sci. 430 (2018) 208–217.
[16] J. Jing, S. Cao, C. Hu, C. Chen, A comparison study of alkali metal-doped g-C_3N_4 for visible-light photocatalytic hydrogen evolution, Chin. J. Catal. 38 (2017) 1981–1989.
[17] F. Xing, Q. Liu, M. Song, C. Huang, Fluorine modified boron carbon nitride semiconductors for improved photocatalytic CO_2 reduction under visible light, ChemCatChem 10 (2018) 5270–5279.
[18] N. Ning, L. Zhang, J. Fu, B. Cheng, J. Yu, Self-assembled hierarchical direct Z-scheme g-C_3N_4/ZnO microspheres with enhanced photocatalytic CO_2 reduction performance, Appl. Surf. Sci. 441 (2018) 12–22.
[19] K.U.R. Naveed, L. Wang, H.J. Yu, R.S. Ullah, M. Haroon, S. Fahad, J.Y. Li, T. Elshaarani, R.U. Khan, A. Nazir, Recent progress in the electron paramagnetic resonance study of polymers, Polym. Chem. 9 (2018) 3306–3335.
[20] N.M. Atherton, Electron Spin Resonance: Theory and Applications, Wiley: Halsted Press, Chichester, New York, 1973.
[21] J. Sun, J. Zhang, M. Zhang, M. Antonietti, X. Fu, X. Wang, Bioinspired hollow semiconductor nanospheres as photosynthetic nanoparticles, Nat. Commun. (2012) 1139.
[22] I. Papailias, N. Todorova, T. Giannakopoulou, S. Karapati, N. Boukos, D. Dimotikali, C. Trapalis, Enhanced NO_2 abatement by alkaline-earth modified g-C_3N_4 nanocomposites for efficient air purification, Appl. Surf. Sci. 430 (2018) 225–233.
[23] L. Yang, P. Wang, J. Yin, C. Wang, G. Dong, Y. Wang, W. Ho, Engineering of reduced graphene oxide on nanosheet g-C_3N_4/perylene imide heterojunction for enhanced photocatalytic redox performance, Appl. Catal. B-Environ. 250 (2019) 42–51.
[24] Y. Shi, J. Huang, G. Zeng, Stable, metal-free, visible-light-driven photocatalyst for efficient removal of pollutants mechanism of action, 531 (2018) 433–443.
[25] Y. Zhao, X. Liang, Y. Wang, H. Shi, E. Liu, J. Fan, X. Hu, Degradation and removal of ceftriaxone sodium in aquatic environment with Bi_2WO_6/g-C_3N_4 photocatalyst, J. Colloid Interf. Sci. 523 (2018) 237–247.
[26] D. Xu, B. Cheng, W. Wang, C. Jiang, J. Yu, Ag_2CrO_4/g-C_3N_4/graphene oxide ternary nanocomposite Z-scheme photocatalyst with enhanced CO_2 reduction activity, Appl. Catal. B-Environ. 231 (2018) 368–380.
[27] X. She, L. Liu, H. Ji, Z. Mo, Y. Li, L. Huang, D. Du, H. Xu, H. Li, Template-free synthesis of 2D porous ultrathin nonmetal-doped g-C_3N_4 nanosheets with highly efficient photocatalytic H_2 evolution from water under visible light, Appl. Catal. B-Environ. 187 (2016) 144–153.
[28] W. Yu, D. Xu, T. Peng, Enhanced photocatalytic activity of g-C_3N_4 for selective CO_2 reduction to CH_3OH via facile coupling of ZnO: a direct Z-scheme mechanism, J. Mater. Chem. A 3 (2015) 19936–19947.
[29] M. Hatem, C. Bilel, G. Thomas, B. Lavinia, M. Kevin, M. Ghouti, S. Rapha, Growth of ZnO nanorods on graphitic carbon nitride g-C_3N_4 sheets for the preparation of photocatalysts with high visible-light activity, ChemCatChem 10 (2018) 4987–4997.
[30] L. Zhang, Q.Q. Liu, Y.Y. Chai, J. Ren, W.L. Dai, Imidazole modified g-C_3N_4 photocatalyst: structural characterization and versatile energy applications, Appl. Surf. Sci. 430 (2018) 316–324.
[31] M. Liu, P. Xia, L. Zhang, B. Cheng, J. Yu, Enhanced photocatalytic H_2-production activity of g-C_3N_4 nanosheets via optimal photodeposition of Pt as cocatalyst, ACS Sustain. Chem. Eng. 6 (2018) 10472–10480.
[32] F. Chen, H. Yang, W. Luo, P. Wang, H. Yu, Selective adsorption of thiocyanate anions on Ag-modified g-C_3N_4 for enhanced photocatalytic hydrogen evolution, Chin. J. Catal. 38 (2018) 1990–1998.
[33] B. Zhu, P. Xia, W. Ho, J. Yu, Isoelectric point and adsorption activity of porous g-C_3N_4, Appl. Surf. Sci. 344 (2015) 188–195.
[34] W. Yu, S. Zhang, J. Chen, P. Xia, M. Richter, L. Chen, W. Xu, J. Jin, S. Chen, T. Peng, Biomimetic Z-scheme photocatalyst with a tandem solid-state electron flow catalyzing H_2 evolution, J. Mater. Chem. A 6 (2018) 15668–15674.
[35] J. Fu, C. Bie, B. Cheng, C. Jiang, J. Yu, Hollow CoS_x polyhedrons act as high-efficiency cocatalyst for enhancing the photocatalytic hydrogen generation of g-C_3N_4, ACS Sustain. Chem. Eng. 6 (2018) 2767–2779.
[36] Z. Yunqing, W. Tian, X. Tao, L. Yingxuan, W. Chuanyi, Size effect of Pt co-catalyst on photocatalytic efficiency of g-C_3N_4 for hydrogen evolution, Appl. Surf. Sci. 464 (2018) 36–42.
[37] Y. Fu, Z. Li, Q. Liu, X. Yang, T. Hua, Construction of carbon nitride and MoS_2 quantum dot 2D/0D hybrid photocatalyst: direct Z-scheme mechanism for improved photocatalytic activity, Chin. J. Catal. 38 (2017) 2160–2170.
[38] H. Wu, S. Bandaru, J. Liu, L. Li, Z. Wang, Adsorption of H_2O, H_2, O_2, CO, NO, and CO_2 on graphene g-C_3N_4 nanocomposite investigated by density functional theory, Appl. Surf. Sci. 430 (2018) 125–136.
[39] B. Jirong, Y. Chaochuang, X. Haiyang, C. Gang, N. Zhijiang, W. Zhilei, L. Yaguang, K. Shifei, Z. Zheng, L. Xi, Facile urea-assisted precursor pre-treatment to fabricate porous g-C_3N_4 nanosheets for remarkably enhanced visible-light-driven hydrogen evolution, J. Colloid Interf. Sci. 532 (2018) 280–286.
[40] Q. Xu, B. Zhu, C. Jiang, B. Cheng, J. Yu, Constructing 2D/2D Fe_2O_3/g-C_3N_4 direct Z-scheme photocatalysts with enhanced H_2 generation performance, Solar RRL 2 (2018) 1800006.
[41] D.C. Wei, Y.Q. Liu, Y. Wang, H.L. Zhang, L.P. Huang, G. Yu, Synthesis of N-doped graphene by chemical vapor deposition and its electrical properties, Nano Lett. 9 (2009) 1752–1758.
[42] S.M. Ren, M.J. Cui, W.S. Li, J.B. Pu, Q.J. Xue, L.P. Wang, N-doping of graphene: toward long-term corrosion protection of Cu, J. Mater. Chem. A 6 (2018) 24136–24148.
[43] Y. Zhu, C. Xiong, S. Song, Z. Le, S.J. Jiang, Coordination-driven synthesis of perfected pi-conjugated graphitic carbon nitride with efficient charge transfer for

oxygen activation and gas purification, 538 (2018) 237–247.
[44] J.S. Zhang, M.W. Zhang, R.Q. Sun, X.C. Wang, A facile band alignment of polymeric carbon nitride semiconductors to construct isotype heterojunctions, Angew. Chem. Int. Edit. 51 (2012) 10145–10149.
[45] J.S. Zhang, G.G. Zhang, X.F. Chen, S. Lin, L. Mohlmann, G. Dolega, G. Lipner, M. Antonietti, S. Blechert, X.C. Wang, Co-monomer control of carbon nitride semiconductors to optimize hydrogen evolution with visible light, Angew. Chem. Int. Edit. 51 (2012) 3183–3187.
[46] W. Ho, Z. Zhang, W. Lin, S. Huang, X. Zhang, X. Wang, Y. Huang, Copolymerization with 2,4,6-triaminopyrimidine for the rolling-up the layer structure, tunable electronic properties, and photocatalysis of g-C_3N_4, ACS Appl. Mater. Interfaces 7 (2015) 5497–5505.
[47] B. Zhu, L. Zhang, B. Cheng, J. Yu, First-principle calculation study of tri-s-triazine-based g-C_3N_4: a review, Appl. Catal. B-Environ. 224 (2017) 983–999.
[48] J. Liu, C. Bei, New understanding of photocatalytic properties of Zigzag and Armchair g-C_3N_4 Nanotubes from electronic structures and carrier effective mass, Appl. Surf. Sci. 430 (2018) 348–354.
[49] B. Zhu, L. Zhang, D. Xu, B. Cheng, J. Yu, Adsorption investigation of CO_2 on g-C_3N_4 surface by DFT calculation, J. CO2 Util. 21 (2017) 327–335.
[50] B. Zhu, J. Zhang, C. Jiang, B. Cheng, J. Yu, First principle investigation of halogen-doped monolayer g-C_3N_4 photocatalyst, Appl. Catal. B-Environ. 207 (2017) 27–34.
[51] T. Tong, B.W. He, B.C. Zhu, B. Cheng, L.Y. Zhang, First-principle investigation on charge carrier transfer in transition-metal single atoms loaded g-C_3N_4, Appl. Surf. Sci. 459 (2018) 385–392.
[52] L. Shi, Z. Li, K. Marcus, G.Z. Wang, K. Liang, W.H. Niu, Y. Yang, Integration of Au nanoparticles with a g-C3N4 based heterostructure: switching charge transfer from type-II to Z-scheme for enhanced visible light photocatalysis, Chem. Commun. 54 (2018) 3747–3750.
[53] S. Fanfei, T. Siyu, Z. Hao, X. Zipeng, Y. Ruoou, M. Bingbao, J. Zheng, Uniform Pt quantum dots-decorated porous g-C_3N_4 nanosheets for efficient separation of electron-hole and enhanced solar-driven photocatalytic performance, J. Colloid Interf. Sci. 531 (2018) 119–125.
[54] J. Fu, J. Yu, C. Jiang, B. Cheng, G-C_3N_4-based heterostructured photocatalysts, Adv. Energy Mater. 8 (2018) 1701503.
[55] Y.J. Cai, D.Y. Li, J.Y. Sun, M.D. Chen, Y.R. Li, Z.W. Zou, H. Zhang, H.M. Xu, D.S. Xia, Synthesis of BiOCl nanosheets with oxygen vacancies for the improved photocatalytic properties, Appl. Surf. Sci. 439 (2018) 697–704.
[56] K. Jungwon, L. Chulwee, C. Wonyong, Platinized WO_3 as an environmental photocatalyst that generates OH radicals under visible light, Environ. Sci. Technol. 44 (2010) 6849–6854.
[57] Y.Z. Hong, Y.H. Jiang, C.S. Li, W.Q. Fan, X. Yan, M. Yan, W.D. Shi, In-situ synthesis of direct solid-state Z-scheme V_2O_5/g-C_3N_4 heterojunctions with enhanced visible light efficiency in photocatalytic degradation of pollutants, Appl. Catal. B-Environ. 180 (2016) 663–673.
[58] K.H. Leong, P.F. Lim, L.C. Sim, V. Punia, S. Pichiah, Improved solar light stimulated charge separation of g-C_3N_4 through self-altering acidic treatment, Appl. Surf. Sci. 430 (2018) 355–361.
[59] F. Dong, Z. Wang, Y. Li, W.K. Ho, S.C. Lee, Immobilization of polymeric g-C_3N_4 on structured ceramic foam for efficient visible light photocatalytic air purification with real indoor illumination, Environ. Sci. Technol. 48 (2014) 10345–10353.
[60] X. She, J. Wu, H. Xu, J. Zhong, Y. Wang, Y. Song, K. Nie, Y. Liu, Y. Yang, M.T.F. Rodrigues, High efficiency photocatalytic water splitting using 2D α-Fe_2O_3/g-C_3N_4 Z-scheme catalysts, Adv. Energy Mater. 7 (2017) 1700025.
[61] Y.S. Cheng, O.S. Xin, G. Jun, Y. Ming, F.J. Yong, F.X. Xing, W.L. Juan, L.Z. Sheng, Y.J. Hua, Z. Yong, A room-temperature reactive-template route to mesoporous $ZnGa_2O_4$ with improved photocatalytic activity in reduction of CO_2, Angew. Chem. Int. Edit. 122 (2010) 6544–6548.
[62] T.K. Townsend, E.M. Sabio, N.D. Browning, F.E. Osterloh, Photocatalytic water oxidation with suspended alpha-Fe_2O_3 particles–effects of nanoscaling, Energy Environ. Sci. 4 (2011) 4270–4275.